depending on the particle or hole character of the larger intragap state, respectively. Such different quantum systems coexist and alternate between neighboring molecules because of their high localization at the impurity site.

The MnPc molecular superstructure thus represents a useful nanoscopic workbench where magnetic coupling with the substrate can be measured from the alignment of the bound states and tuned by choosing the appropriate molecule. The interaction of these bound states with other intragap excitations [e.g., multiple Andreev reflections in contact junctions (*25*–*27*)] or with superconductors with other symmetries [e.g., p-wave (*28*–*30*)] represents a fascinating application of this study to ongoing problems in condensed-matter physics.

References and Notes

1. J. Kondo, *Prog. Theor. Phys.* **32**, 37 (1964).
2. L. Yu, *Acta Phys. Sin.* **21**, 75 (1965).
3. H. Shiba, *Prog. Theor. Phys.* **40**, 435 (1968).
4. A. I. Rusinov, *Zh. Eksp. Teor. Fiz.* **56**, 2047 (1969) [*Sov. Phys. JETP* **29**, 1101 (1969)].
5. A. V. Balatsky, I. Vekhter, J.-X. Zhu, *Rev. Mod. Phys.* **78**, 373 (2006).
6. A. Yazdani, B. A. Jones, C. P. Lutz, M. F. Crommie, D. M. Eigler, *Science* **275**, 1767 (1997).
7. S.-H. Ji *et al.*, *Phys. Rev. Lett.* **100**, 226801 (2008).
8. C. P. Moca, E. Demler, B. Janko, G. Zarand, *Phys. Rev. B* **77**, 174516 (2008).
9. M. E. Flatté, J. M. Byers, *Phys. Rev. B* **56**, 11213 (1997).
10. M. Flatté, J. Byers, *Phys. Rev. Lett.* **78**, 3761 (1997).
11. M. R. Buitelaar, T. Nussbaumer, C. Schönenberger, *Phys. Rev. Lett.* **89**, 256801 (2002).
12. M. I. Salkola, A. V. Balatsky, J. R. Schrieffer, *Phys. Rev. B* **55**, 12648 (1997).
13. T. Matsuura, *Prog. Theor. Phys.* **57**, 1823 (1977).
14. O. Sakai, Y. Shimizu, H. Shiba, K. Satori, *J. Phys. Soc. Jpn.* **62**, 3181 (1993).
15. Materials and methods are available as supporting material on *Science* Online.
16. V. Madhavan V, W. Chen, T. Jamneala, M. F. Crommie, N. S. Wingreen, *Science* **280**, 567 (1998).
17. J. Li, W.-D. Schneider, R. Berndt, B. Delley, *Phys. Rev. Lett.* **80**, 2893 (1998).
18. Y.-S. Fu *et al.*, *Phys. Rev. Lett.* **99**, 256601 (2007).
19. S.-H. Ji *et al.*, *Chin. Phys. Lett.* **27**, 087202 (2010).
20. J. J. Parks *et al.*, *Science* **328**, 1370 (2010).
21. A. Posazhennikova, P. Coleman, *Phys. Rev. Lett.* **94**, 036802 (2005).
22. The crossing point differs from the estimated value $k_B \cdot T_K/\Delta \sim 0.3$ (*13*, *14*). Recent renormalization group theory calculations find that the quantum phase transition may vary depending on the parameters (*31*). We note that the more complex double Kondo state of MnPc may influence the transition.
23. M.-S. Liao, J. D. Watts, M.-J. Huang, *Inorg. Chem.* **44**, 1941 (2005).
24. L. Gao *et al.*, *Phys. Rev. Lett.* **99**, 106402 (2007).
25. M. Ternes *et al.*, *Phys. Rev. B* **74**, 132501 (2006).
26. A. Eichler *et al.*, *Phys. Rev. Lett.* **99**, 126602 (2007).
27. T. Sand-Jespersen *et al.*, *Phys. Rev. Lett.* **99**, 126603 (2007).
28. G. E. Volovik, *JEPTP Lett.* **70**, 609 (1999).
29. N. Read, D. Green, *Phys. Rev. B* **61**, 10267 (2000).
30. D. A. Ivanov, *Phys. Rev. Lett.* **86**, 268 (2001).
31. J. Bauer, A. Oguri, A. C. Hewson, *J. Phys. Condens. Matter* **19**, 486211 (2007).
32. I. Horcas *et al.*, *Rev. Sci. Instrum.* **78**, 013705 (2007).

Acknowledgments: We thank F. von Oppen and A. Strozecka for stimulating discussions and E.K.U. Gross for motivating us to study this topic. This research was supported by the Focus area "Nanoscale Materials" of the Freie Universität Berlin and by the Deutsche Forschungsgemeinschaft through the collaborative projects Sfb 658 and SPP 1243.

Supporting Online Material

www.sciencemag.org/cgi/content/full/332/6032/940/DC1
Materials and Methods
Figs. S1 to S4

27 December 2010; accepted 6 April 2011
10.1126/science.1202204

Chlorinated Indium Tin Oxide Electrodes with High Work Function for Organic Device Compatibility

M. G. Helander,[1*†] Z. B. Wang,[1*†] J. Qiu,[1] M. T. Greiner,[1] D. P. Puzzo,[1] Z. W. Liu,[1*] Z. H. Lu[1,2*]

In organic light-emitting diodes (OLEDs), a stack of multiple organic layers facilitates charge flow from the low work function [~4.7 electron volts (eV)] of the transparent electrode (tin-doped indium oxide, ITO) to the deep energy levels (~6 eV) of the active light-emitting organic materials. We demonstrate a chlorinated ITO transparent electrode with a work function of >6.1 eV that provides a direct match to the energy levels of the active light-emitting materials in state-of-the art OLEDs. A highly simplified green OLED with a maximum external quantum efficiency (EQE) of 54% and power efficiency of 230 lumens per watt using outcoupling enhancement was demonstrated, as were EQE of 50% and power efficiency of 110 lumens per watt at 10,000 candelas per square meter.

Transparent tin-doped indium oxide (ITO) electrodes are used in several classes of devices, including liquid crystal displays, organic photovoltaics, and organic light-emitting diodes (OLEDs) (*1*–*11*). Despite the dominance of ITO in the flat-panel display industry, its surface electronic properties are less than ideal for organic devices. In particular, the low work function of ITO complicates the design of organic optoelectronic devices in terms of charge injection from the electrodes because of the large mismatch between the low work function of ITO (~4.7 eV) and the energy levels of the active organic materials used in devices (*12*, *13*) (typically 5.7 to 6.3 eV). For example, the highest occupied molecular orbital (HOMO) of commonly used host materials in state-of-the-art phosphorescent OLEDs is typically ~6 eV, which is much too deep to directly inject charge from ITO.

As a result, multiple transport layers are required to match the energy levels in a stepwise fashion. An additional injection layer is also typically used, with the most common examples being copper phthalocyanine (*14*), poly(3,4-ethylenedioxythiophene) (PEDOT) (*15*), transition-metal oxides (*16*), or p-doped organic layers (*17*–*19*). Each additional layer that is required greatly increases the manufacturing costs and also introduces additional hetero-junctions into the device that can be detrimental to device stability and performance (*20*, *21*). A transparent electrode with a tunable high work function that matches the energy levels of the active organic material would avoid the requirement for multiple transport and injection layers.

To address this issue, we functionalized the surface of ITO with a controlled amount of electronegative halogen atoms that were derived from an inert halogenated solvent precursor that was activated with ultraviolet (UV) radiation. An air-stable electrode with a work function greater than 6.1 eV was achieved in the case of chlorinated ITO (Cl-ITO) without altering the surface roughness, transparency, and conductivity of the electrode. The tunable high work function enabled the fabrication of a highly simplified OLED with a high efficiency and brightness.

To fabricate Cl-ITO, we placed bare substrates in a closed Pyrex reaction vessel with *o*-dichlorobenzene and treated them with UV radiation from a low-pressure mercury lamp (SEN Lights PL16-110) for up to 10 min [see (*22*) for details]. Cl radicals liberated from the solvent displaced oxygen on the surface of the electrode. After treatment with UV radiation, the substrates were exposed to UV-generated ozone for an additional 3 min to fully oxidize any residual chlorocarbon fragments on the surface (fig. S3). X-ray photoelectron spectroscopy (XPS) was used to characterize the work function and surface composition of the Cl-ITO electrode. The secondary electron cut-off of Cl-ITO as a function of increasing UV treatment time from 0 to 10 min monotonically shifted to lower binding energy, indicating an increase in work function (Fig. 1A). The intensity of the Cl 2p peak (Fig. 1B)

[1]Department of Materials Science and Engineering, University of Toronto, 184 College Street, Toronto, Ontario, Canada M5S 3E4. [2]Department of Physics, Yunnan University, 2 Cuihu Beilu, Yunnan, Kunming 650091, People's Republic of China.

*To whom correspondence should be addressed. E-mail: michael.helander@utoronto.ca (M.G.H.); zhibin.wang@utoronto.ca (Z.B.W.); zhiwei.liu@utoronto.ca (Z.W.L); zhenghong.lu@utoronto.ca (Z.H.L)
†These authors contributed equally to this work.

also increased with treatment time, indicating an increase in the surface coverage of Cl. Beyond 10 min of treatment time, the secondary electron cut-off and Cl 2p peak remained unchanged, suggesting that the surface was saturated with Cl.

To determine the distribution of Cl atoms in the Cl-ITO, we performed angle-resolved XPS (AR-XPS) measurements on a sample treated for 10 min. The measured intensities of the Cl 2p (from the overlayer) and In 3d (from the substrate) core levels as a function of photoelectron take-off angle (θ) are shown in Fig. 1C. The surface sensitivity of XPS increases at low photoelectron take-off angles because of a reduction in photoelectron escape depth. Hence, the increase in signal intensity of the Cl 2p core level at low photoelectron take-off angles indicates that the Cl atoms are confined to the surface of the Cl-ITO. The AR-XPS data also indicate that the surface coverage of Cl is close to one monolayer for the Cl-saturated surface (*23*).

The work function determined from the secondary electron cut-off as a function of surface coverage Θ (determined from the Cl 2p signal intensity and AR-XPS results) increased linearly with the Cl surface coverage (Fig. 1D). For the highest Cl surface coverage (Θ ≈ 1), corresponding to a treatment time of 10 min, we measured a work function of 6.13 eV. This value is particularly high considering that the electrode is prepared in ambient air. The high work function was also found to be stable with time, changing less than 2% after 24 hours.

The C 1s, Cl 2s, and Cl 2p core levels of Cl-ITO with Θ = 0 (bare surface) and Θ ≈ 1 (saturated surface) are shown in Fig. 2A. The C 1s peak is essentially identical on the two samples, indicating that the Cl was not in the form of a chloro-carbon fragment. We have also confirmed that the Cl is not from residual chlorinated solvent on the surface by measuring a sample dipped into chlorinated solvent; no Cl was detected (fig. S4). This finding suggests that the Cl is chemically bonded to the surface. To determine the nature of the Cl chemical bond we examined high-resolution XPS spectra of the Cl 2p core level and found that it could be fit using a single doublet peak (fig. S5), which indicates that only a single chemical species of Cl is present. The Cl $2p_{3/2}$ binding energy of this species is 199.06 eV, which rules out chlorate and perchlorate (*24*). The Cl 2p core level of Cl-ITO and $InCl_3$ are identical (Fig. 2B), which demonstrates that the Cl is bonded to In at the surface. We could not resolve a separate peak in the In 3d core level for the In-Cl bond because of the similarity in binding energies between In-O and In-Cl. Also, it is unlikely that the Cl bonds to Sn as tin chloride is readily hydrolyzed to tin oxide upon exposure to air.

Figure 2C shows the valence band of Cl-ITO with Θ = 0 (bare surface) and Θ ≈ 1 (saturated surface) measured with XPS and ultraviolet photoelectron spectroscopy (UPS). The valence band maximum of both samples is located 3.1 eV below the Fermi level (E_F), indicating that the Cl does not alter the doping level. Because ITO is an *n*-type degenerate semiconductor, the finite density of states (DOS) at E_F is representative of the partially filled conduction band. The DOS at E_F, which is a sensitive indication of surface electronic structure, is nearly identical on both samples. The high work function of Cl-ITO cannot be a result of a change in E_F (i.e., electrochemical potential), doping level, or surface electronic structure. By definition, the work function of a uniform surface of a conductor is the difference between the electrochemical potential $\bar{\mu}$ of electrons in the bulk and the electrostatic potential energy $-e\Phi_{vac}$ of an electron in the vacuum just outside the surface (*25*)

$$e\phi_m = -e\Phi_{vac} - \bar{\mu} \quad (1)$$

The Cl must change the electrostatic potential just outside the surface. Our XPS data show that Cl is bonded to In at the surface. The large difference in electronegativity between In and Cl (i.e., 1.78 compared to 3.16) means that the In-Cl bonds at the surface are polar, which is equivalent to introducing a layer of dipoles across the surface. These dipoles would increase the electrostatic potential energy just outside the surface, resulting in a much higher work function (fig. S6).

To demonstrate the benefits of the tunable high work function of Cl-ITO for device applications, we fabricated simplified phosphorescent OLEDs using the high work function of Cl-ITO

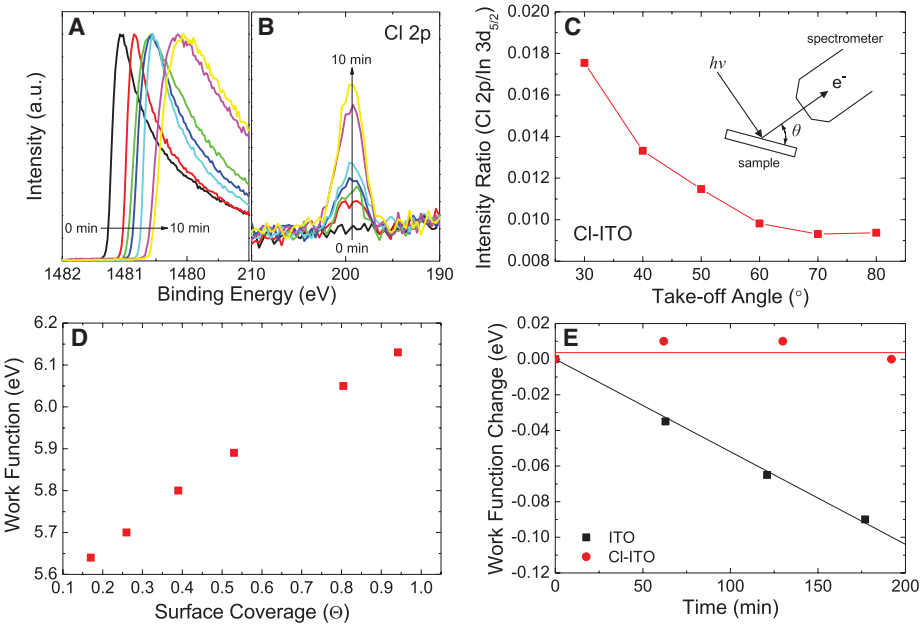

Fig. 1. Work function and Cl surface coverage. (**A**) Secondary electron cut-off and (**B**) Cl 2p peak as a function of increasing UV treatment time. (**C**) Angle-resolved XPS measurements showing the Cl 2p/In $3d_{5/2}$ intensity ratio of Cl-ITO as a function of photoelectron take-off angle (θ). The inset shows the measurement geometry. (**D**) Work function as a function of Cl surface coverage (Θ); Θ = 1.0 corresponds to one monolayer. (**E**) Change in work function of Cl-ITO and ITO as a function of time. The lines are a guide for the eye.

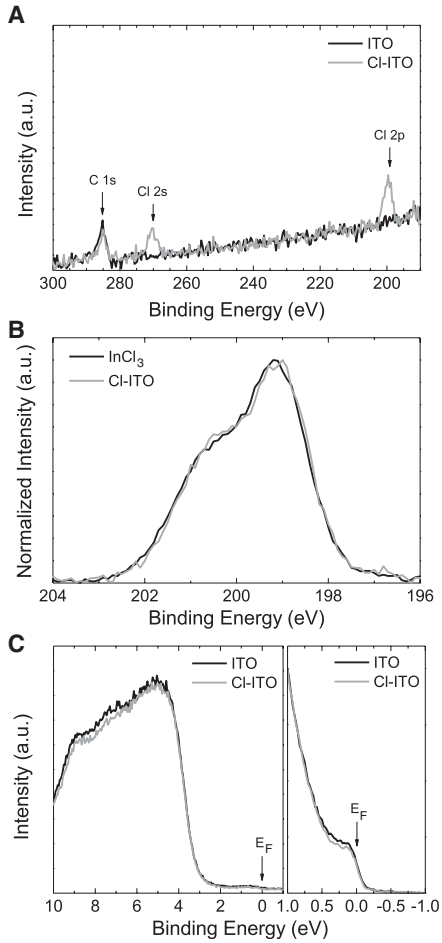

Fig. 2. Surface composition of Cl-ITO. (**A**) C 1s, Cl 2s, and Cl 2p core levels for Θ = 0 (bare surface) and Θ ≈ 1 (saturated surface). (**B**) The Cl 2p core level of Cl-ITO compared to $InCl_3$. (**C**) (Left) Valence band for Θ = 0 and Θ ≈ 1, and (right) density of states at the Fermi level (E_F) for Θ = 0 and Θ ≈ 1.

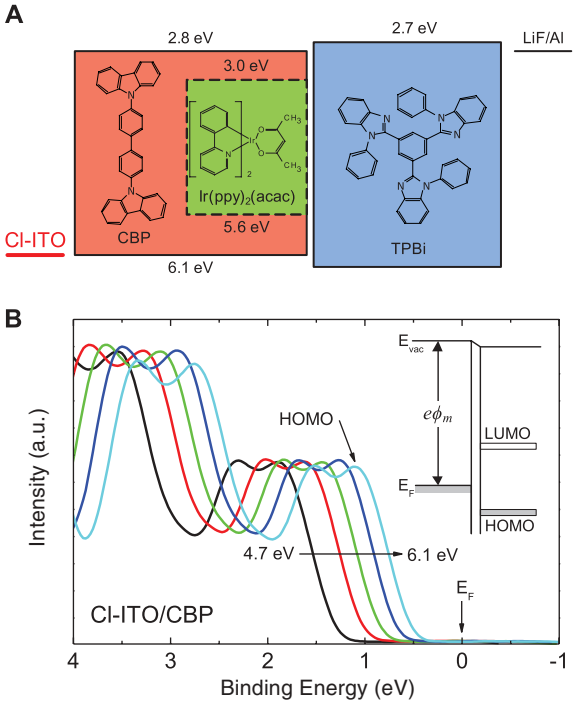

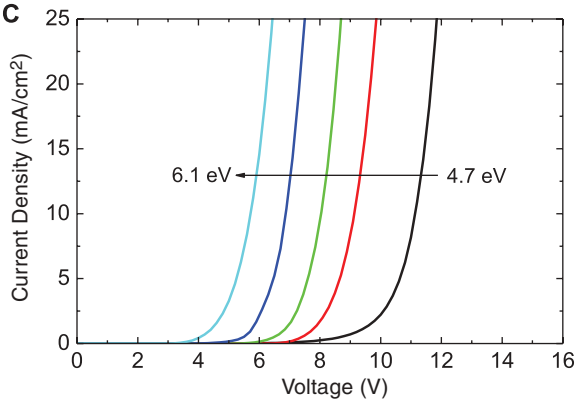

Fig. 3. Energy-level alignment between Cl-ITO and CBP. (**A**) Schematic energy-level diagram of the simplified OLED: Cl-ITO/CBP (35 nm)/CBP:Ir(ppy)$_2$(acac) (15 nm, 8%)/TPBi (65 nm)/LiF (1 nm)/Al (100 nm). (**B**) UPS spectra of CBP deposited on Cl-ITO with different work function. The inset shows a schematic energy-level diagram of the Cl-ITO/CBP interface. LUMO, lowest unoccupied molecular orbital. (**C**) Current density as a function of voltage for CBP-based OLEDs fabricated on Cl-ITO with different work function.

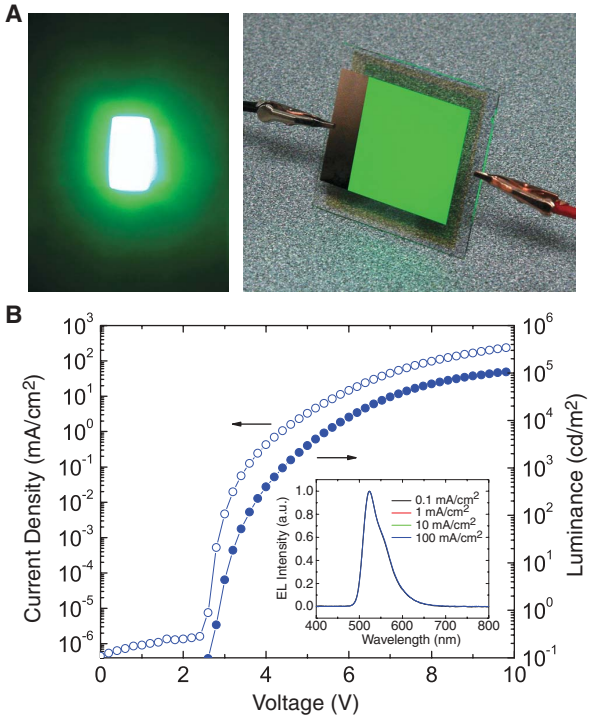

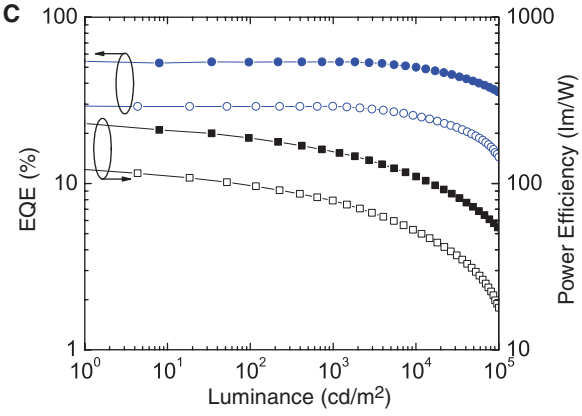

Fig. 4. Device performance of OLEDs with Cl-ITO electrode. (**A**) (Left) Photograph of a device (1 mm by 2 mm) operating at a high brightness of 5000 cd/m^2 and (right) a large-area prototype device (50 mm by 50 mm). (**B**) Current density and luminance as a function of voltage. The inset shows the EL spectra as a function of current density. (**C**) EQE and power efficiency as a function of luminance. The open symbols are without outcoupling enhancement, and the solid symbols are with lens-based outcoupling enhancement.

to enable direct injection of holes into 4,4′-*N*,*N*′-dicarbazole-biphenyl (CBP), the host material used for the phosphorescent emitter. A complex multilayer hole injection and transport stack is typically required to match the deep HOMO of CBP (6.1 eV). Using Cl-ITO, however, allows us to tune the work function of the anode to match the deep HOMO of CBP without having to introduce any additional injection and transport layers, thus greatly simplifying the device design and fabrication. Such a simplified device design also has the potential to greatly improve device performance because it eliminates several of the heterojunctions in the device that can block carrier transport and contribute to exciton quenching (*21*).

A schematic energy-level diagram of the simplified OLED with Cl-ITO as an anode is shown in Fig. 3A, in which part of the CBP layer is doped with the phosphorescent emitter to form the emission zone. The HOMO-derived peak of CBP deposited on Cl-ITO with different work functions measured with UPS (Fig. 3B) shows that by tuning the work function of the Cl-ITO to match the deep ionization potential of the CBP, the barrier height at the interface can be reduced by ~0.7 eV. The current density as a function of voltage of OLEDs fabricated on Cl-ITO with

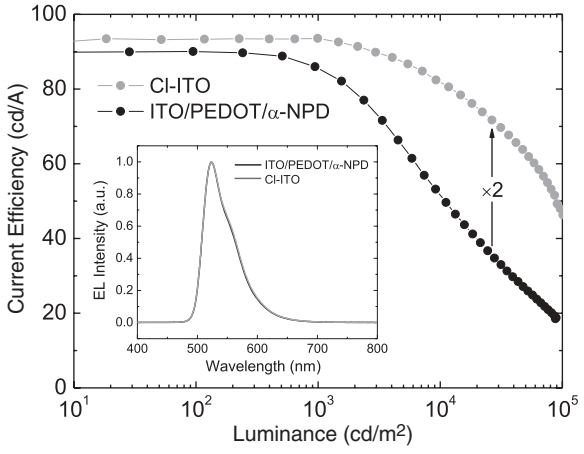

Fig. 5. Effect of stepwise injection on device performance. Current efficiency as a function of luminance for devices with Cl-ITO anode in comparison to devices using a traditional stepwise injection structure. The ITO was coated with 5 nm of PEDOT, and the 35-nm-thick undoped region of CBP was replaced with a separate layer of α-NPD of the same thickness, yielding ITO/PEDOT (5 nm)/α-NPD (35 nm)/CBP:Ir(ppy)$_2$(acac) (15 nm, 8%)/TPBi (65 nm)/LiF (1 nm)/Al (100 nm).

different work functions is shown in Fig. 3C. With increasing work function, the operating voltage of the OLED was markedly reduced because of the lower barrier height at the Cl-ITO/CBP interface as shown by the UPS results. Photographs of a Cl-ITO–based green-emitting OLED operating at high brightness, as well as a large-area prototype device, are shown in Fig. 4A, and the current-voltage-luminance characteristics of an optimized device with a Cl-ITO anode is shown in Fig. 4B (the white-looking emission is due to the high brightness of the OLED saturating the detector of the camera). A reference device fabricated on ITO (same organic layer structure) exhibited an extremely high driving voltage and no visible electroluminescence (EL) in the voltage range tested because of the poor energy-level matching between ITO and CBP. The external quantum efficiency (EQE) of the Cl-ITO device (Fig. 4C) reaches 29.1% (93 cd/A) at 100 cd/m^2, 29.2% (94 cd/A) at 1000 cd/m^2, and 25.4% (81 cd/A) at 10,000 cd/m^2. Although a similarly high efficiency can be achieved in a traditional device with *N*,*N*′-diphenyl-*N*,*N*′-bis-(1-naphthyl)-1-1′-biphenyl-4,4′-diamine (α-NPD) hole-transport layer and PEDOT hole-injection layer at low luminance (90 cd/A at 100 cd/m^2), the efficiency is much lower at high luminance (50 cd/A at 10,000 cd/m^2), as shown in Fig. 5. The drastic efficiency roll-off in the traditional device (i.e., ITO/PEDOT/α-NPD) is due to the additional organic-organic heterojunctions in the device, which block carrier transport and contribute to exciton quenching (*21*). Even at an ultrahigh luminance of 100,000 cd/m^2, the EQE of the Cl-ITO device is still as high as 14.3% (46 cd/A). The power efficiency of the Cl-ITO device reaches 97 lm/W at 100 cd/m^2, 79 lm/W at 1000 cd/m^2, and 51 lm/W at 10,000 cd/m^2, which is better than state-of-the-art *p-i-n* phosphorescent organic light-emitting diodes, which require six or more organic layers (*19*, *26*).

The use of a simple lens-based structure to help outcouple trapped light at the glass-air interface (*7*, *8*) can further enhance the device performance, and the EQE can be further increased to 54% at 1000 cd/m^2, 50% at 10,000 cd/m^2, and 35% at 100,000 cd/m^2. The maximum power efficiency is also increased to 230 lm/W. At 10,000 cd/m^2 the power efficiency is still as high as 110 lm/W, more than double the value of the best previously reported OLED (*27*). These high efficiencies are achieved with a simplified device design using readily available materials and without using chemically doped layers. Using a high-index substrate instead of glass could further help to improve the efficiency by outcoupling more light trapped in the ITO modes (*7*, *28*).

References and Notes

1. J. Kido, M. Kimura, K. Nagai, *Science* **267**, 1332 (1995).
2. Z. Shen, P. Burrows, V. Bulovic, S. Forrest, M. Thompson, *Science* **276**, 2009 (1997).
3. R. H. Friend *et al.*, *Nature* **397**, 121 (1999).
4. M. A. Baldo, M. E. Thompson, S. R. Forrest, *Nature* **403**, 750 (2000).
5. C. D. Müller *et al.*, *Nature* **421**, 829 (2003).
6. Y. Sun *et al.*, *Nature* **440**, 908 (2006).
7. S. Reineke *et al.*, *Nature* **459**, 234 (2009).
8. Y. Sun, S. R. Forrest, *Nat. Photonics* **2**, 483 (2008).
9. M. D. Irwin, D. B. Buchholz, A. W. Hains, R. P. H. Chang, T. J. Marks, *Proc. Natl. Acad. Sci. U.S.A.* **105**, 2783 (2008).
10. T. Sekitani *et al.*, *Nat. Mater.* **8**, 494 (2009).
11. W. H. Koo *et al.*, *Nat. Photonics* **4**, 222 (2010).
12. N. R. Armstrong, P. A. Veneman, E. Ratcliff, D. Placencia, M. Brumbach, *Acc. Chem. Res.* **42**, 1748 (2009).
13. X. H. Sun *et al.*, *Chem. Phys. Lett.* **370**, 425 (2003).
14. S. A. Van Slyke, C. H. Chen, C. W. Tang, *Appl. Phys. Lett.* **69**, 2160 (1996).
15. S. A. Carter, M. Angelopoulos, S. Karg, P. J. Brock, J. C. Scott, *Appl. Phys. Lett.* **70**, 2067 (1997).
16. S. Tokito, K. Noda, Y. Taga, *J. Phys. D* **29**, 2750 (1996).
17. X. Zhou *et al.*, *Appl. Phys. Lett.* **78**, 410 (2001).
18. D. Tanaka *et al.*, *Jpn. J. Appl. Phys.* **46**, L10 (2007).
19. G. He *et al.*, *Appl. Phys. Lett.* **85**, 3911 (2004).
20. H. Aziz, Z. D. Popovic, N. X. Hu, A. M. Hor, G. Xu, *Science* **283**, 1900 (1999).
21. Z. B. Wang *et al.*, *J. Appl. Phys.* **108**, 024510 (2010).
22. Materials and methods are available as supporting material on *Science* Online.
23. S. Oswald, M. Zier, R. Reiche, K. Wetzig, *Surf. Interface Anal.* **38**, 590 (2006).
24. V. I. Nefedov, É. K. Zhumadilov, T. Y. Kopytova, *J. Struct. Chem.* **18**, 549 (1977).
25. C. Herring, M. H. Nichols, *Rev. Mod. Phys.* **21**, 185 (1949).
26. S. Watanabe, N. Ide, J. Kido, *Jpn. J. Appl. Phys.* **46**, 1186 (2007).
27. S.-J. Su, H. Sasabe, Y.-J. Pu, K.-i. Nakayama, J. Kido, *Adv. Mater.* **22**, 3311 (2010).
28. S. Mladenovski, K. Neyts, D. Pavicic, A. Werner, C. Rothe, *Opt. Express* **17**, 7562 (2009).

Acknowledgments: Z.H.L. is a Canada Research Chair in Organic Optoelectronics, Tier I. We acknowledge funding for this research from the Natural Sciences and Engineering Research Council (NSERC) of Canada. We are grateful to T. P. Bender and G. A. Ozin (University of Toronto) for helpful discussions.

Supporting Online Material

www.sciencemag.org/cgi/content/full/science.1202992/DC1
Materials and Methods
Figs. S1 to S14
Tables S1 to S3
References

18 January 2011; accepted 28 March 2011
Published online 14 April 2011;
10.1126/science.1202992

Probing Asthenospheric Density, Temperature, and Elastic Moduli Below the Western United States

Takeo Ito[1,2]* and Mark Simons[1]

Periodic ocean tides continually provide a cyclic load on Earth's surface, the response to which can be exploited to provide new insights into Earth's interior structure. We used geodetic observations of surface displacements induced by ocean tidal loads to constrain a depth-dependent model for the crust and uppermost mantle that provides independent estimates of density and elastic moduli below the western United States and nearby offshore regions. Our observations require strong gradients in both density and elastic shear moduli at the top and bottom of the asthenosphere but no discrete structural discontinuity at a depth of 220 kilometers. The model indicates that the asthenosphere has a low-density anomaly of ~50 kilograms per cubic meter; a temperature anomaly of ~300°C can simultaneously explain this density anomaly and inferred colocated minima in elastic moduli.

Ocean tides on Earth are a well-known phenomenon resulting from periodic variations in gravitational forcing from the Sun and Moon. Variations of density and elastic moduli within Earth's interior control the response to ocean tidal loads (OTLs). Conversely,